A new direct technique for visualizing and measuring gas-liquid mass transfer around bubbles moving in a straight millimetric square channel

Nicolas Dietrich, Karine Loubiere, Miguel Angel Jiménez, Gilles Hébrard, Christophe Gourdon

A new direct technique for visualizing and measuring gas–liquid mass transfer around bubbles moving in a straight millimetric square channel

N. Dietrich [a,b,c,f,*], K. Loubière [d,e,f], M. Jimenez [a,b,c,f], G. Hébrard [a,b,c,f], C. Gourdon [d,e,f]

[a] Université de Toulouse; INSA, UPS, INPT; LISBP, 135 Av. de Rangueil, F-31077 Toulouse, France
[b] INRA UMR 792, Ingénierie des Systèmes Biologiques et des Procédés, F-31400 Toulouse, France
[c] CNRS UMR 5504, Ingénierie des Systèmes Biologiques et des Procédés, F-31400 Toulouse, France
[d] Université de Toulouse, INPT, UPS, Laboratoire de Génie Chimique, 4 allée Emile Monso, BP 84234, 31432 Toulouse, France
[e] CNRS UMR 5503, Laboratoire de Génie Chimique, F-31432 Toulouse, France
[f] Fédération de Recherche FERMAT, CNRS, Toulouse, 31400 Toulouse, France

HIGHLIGHTS

- New colourimetric technique using an oxygen sensitive dye.
- Vizualization of mass transfer around bubbles in millimetric channel.
- Calculation method to determine the transferred oxygen fluxes.
- Tool for quick millireactor design.
- New insight into the mechanism of bubble mass transfer.

GRAPHICAL ABSTRACT

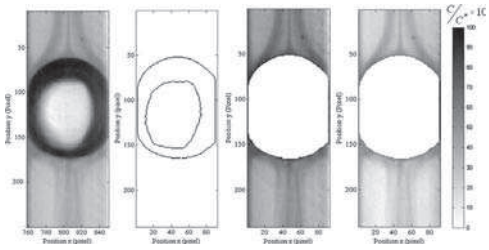

ABSTRACT

The present paper focuses on the local characterization of gas–liquid mass transfer in a straight millimetric square channel, as constituting the preliminary step required for performing gas–liquid reactions in such devices. For this purpose, a new colourimetric technique using an oxygen sensitive dye was developed. It was based on the reduction of a colourimetric indicator in presence of oxygen, this reduction being catalysed by sodium hydroxide and glucose. In this study, resazurin was selected as the colourimetric indicator as it offered various reduced forms, the colours of which ranged from colourless (without oxygen) to pink (when oxygen was present). Thus the mass transfer around bubbles flowing in a straight millimetric square channel could be visualized in space and time. Some pictures were recorded by a monochromatic CCD high speed camera and, after post-processing, the shape, size and velocity of the bubbles, and the grey-level maps around them were measured. A calculation method was also developed to determine the transferred oxygen fluxes around the bubbles and the associated liquid-side mass transfer coefficients. The results compared satisfactorily with global measurements made using oxygen microsensors (Roudet et al., 2011. Hydrodynamics and mass transfer in inertial gas–liquid flow regimes through straigth and meandering millimetric square channels. Chem. Eng. Sci. 66, 2974–2990). This study constitutes a striking example of how interesting a tool this new colourimetric method could be for investigating gas–liquid mass transfer in transparent fluids with a view to quick millireactor design.

Keywords:
Bubble
Mass transfer
Imaging
Multiphase flow
Millichannel
Dissolved oxygen

1. Introduction

Microreaction technology has received much academic and industrial attention as it offers specific advantages (handling and

* Corresponding Author at: Université de Toulouse, 135 avenue de Rangueil, 31077 Toulouse, France. Tel.: +33 561559760; fax: +33 561559760.
E-mail address: Nicolas.Dietrich@insa-toulouse.fr (N. Dietrich).

transport of reduced amounts of fluids, enhancement of heat and mass transfer, high surface-to-volume ratios, smaller disparity of length and time scales, etc.). Applications cover a wide range of domains, especially when gas–liquid systems are involved. For example, they concern the generation of biogas bubbles by anaerobic sludge granules in a bioreactor, bubble nucleation in polymer devolatization processes, micro heat-exchangers, two-phase micro-mixing, fluorination, hydrogenation, biochemical reactions (DNA analysis), materials synthesis, ultrasonic imaging, and photochemical reactions. Whatever the target application, for optimized design of such miniaturized devices, fundamental knowledge related to complex gas–liquid flows and mass transfer mechanisms should be gained first.

For several years, gas–liquid flows in closed microchannels have been the subject of a fast-growing body of literature (for example: Banerjee et al., 1970; Barnea et al., 1983; Thulasidas et al., 1997; Kreutzer et al., 2005; Taha and Cui, 2006; Shao et al., 2009; Gupta et al., 2010). Most of the works deal with understanding and modelling the bubble-train flow of elongated bubbles, as this kind of flow (commonly named Taylor flow) enables good mass transfer rates to be achieved from bubbles to the liquid phase. Some researchers have specifically focused on the quantification of gas–liquid mass transfer in such channels:

- by experiments (for example Bercic and Pintar, 1997; Vandu et al., 2005; Yue et al., 2007; Sobieszuk et al., 2008, 2011); Su et al., 2010; Roudet et al., 2011; Aoki et al., 2011,
- and/or by simulations with Computational Fluid Dynamics software (Van Baten and Krishna, 2004; Gunther et al., 2004; Fries et al., 2008).

An interesting review of this topic can be found in Sobieszuk et al. (2012). The classic experimental methods for measuring the volumetric mass transfer coefficient ($k_l a$) consist of measuring the gas and/or liquid composition (either by means of sensors, or by absorption technique) after a certain time of contact between the two phases. Sobieszuk et al. (2011) have measured the interfacial area using both the Danckwerts chemical method and a photographic method, and have thus determined the film and the cap interfacial areas separately. Tan et al. (2012) have recently developed an online, in-situ method (absorption of CO_2 by NaOH aqueous solution) for segmented gas–liquid flows, in which the mass transfer related to the bubble flow can be determined by measuring the change of gas slug volume. These methods give access only to overall characteristics of gas–liquid mass transfer. First, no distinction is made between the contributions to mass transfer of the bubble formation, bubble flow and phase-separation. Second, no spatial information is available to visualize the locations where the mass transfer from Taylor bubbles occurs. This is known to result from the contributions of the recirculating region between two bubble caps and the film surrounding the bubbles according to

$$k_l a = k_{l,f} \times a_f + k_{l,r} \times a_r \quad (1)$$

The penetration model (Higbie, 1935) is commonly used to calculate the liquid-side mass transfer coefficients from the recirculating region ($k_{l,r}$) and from the liquid film ($k_{l,f}$) by defining the contact time between gas and liquid appropriately for each case (Van Baten and Krishna, 2004). In order to estimate interfacial areas between gas and liquid phases, a hemispherical shape for the bubble nose and rear is generally assumed, with a cylindrical shape for the bubble body. With these assumptions, the specific interfacial area for the liquid film (a_f) and the recirculating region (a_r) can be determined from a knowledge of the channel width and unit cell length.

Such modelling remains difficult to validate experimentally as only bulk measurements are available. The classical method for visualizing gas–liquid mass transfer locally is based on fluorescence quenched by oxygen (François et al., 2011). Its implementation at micro- or millimetric scales is still challenging, mainly because strong light reflections on the complex bubble interface prevent accurate measurements.

To overcome these drawbacks, this paper proposes an original, direct, non-intrusive technique using an oxygen-sensitive dye to quantify the local mass transfer around bubbles flowing in a straight millimetric square channel. The main advantage is that the mass transfer can be visualized without any laser excitation, making this technique easy and user friendly. It is based on the reduction of a colourimetric indicator (resazurin) in presence of oxygen, this reaction being catalysed by sodium hydroxide and glucose.

In a first part, some general principles of the colourimetric technique will be presented, together with the experimental set-up (e.g. the one used by Roudet et al. (2011)) and the methods used (image acquisition). Second, the way to implement this technique will be described, in particular the calibration procedure and the different image processing steps. Results will be expressed in terms of equivalent oxygen concentration field, mass flux of transferred oxygen and liquid-side mass transfer coefficient. They will be discussed with respect to the operating conditions (i.e. liquid and gas superficial velocities), and compared to the measurements obtained by Roudet et al. (2011) inside the same channel.

2. Materials and methods

2.1. General principles of the colourimetric technique

The colourimetric technique is based on the use of an oxygen-sensitive dye. The main advantage is that it is non-intrusive, as the measurements are carried out without disturbing the flow or inserting a physical sensor. There are a large number of organic chemical compounds that present the following properties when subjected to an oxidation/reduction reaction: intense colour in the oxidized or reduced state, and colourless or differently coloured in the conjugate (opposite) state. For example, methylene blue is blue in the oxidized state but colourless in the reduced state. The well-known “blue bottle” experiments use this property (Cook et al., 1994; Walter et al., 1997; Engerer and Gilbert Cook, 1999; Wellman and Noble, 2003). The main drawback when visualizing mass transfer using methylene blue is the slow kinetics of the reactions (Wellman and Noble, 2003). Other redox dyes are available, such as indigo carmine or resazurin, which are, respectively, red and green, and blue and pink in their different forms. The choice of dye mainly depends on two factors:

- the kinetics of the reaction between dissolved oxygen and dye,
- the intensity of the colour generated.

In this study, several dyes were tested: methylene blue, indigo carmine and resazurin. Resazurin was finally chosen because it gave a good compromise between kinetics and colour to be achieved. In addition, resazurin is well-known as its reduction has been used for about 50 years to monitor bacterial and yeast contamination of milk, and also for assessing semen quality (O'Brien et al., 2000).

As shown in Fig. 1, resazurin (blue and not fluorescent) is reduced into resorufin (pink and highly fluorescent), which is itself reduced to dihydroresorufin (colourless and not fluorescent).

These reactions are catalysed by the presence of glucose and sodium hydroxide. In alkaline solutions, glucose is oxidized to D-gluconic acid or alpha-D-gluconolactone:

$$\underset{\text{(Dextrose)}}{HOCH_2(CHOH)_4CHO} + 3OH_- \rightarrow \underset{\text{(Gluconic Acid)}}{HOCH_2(CHOH)_4CO_2} + 2H_2O + 2e^- \quad (2)$$

The change of colour results from the reversible oxidation–reduction reactions between resorufin (pink) and dihydroresorufin (colourless):

$$O_2 + 2.\text{Dihydroresorufin} \rightarrow 2.\text{Resorufin} + 2.H_2O \quad \text{(Fast reaction)} \quad (3)$$

$$\text{Resorufin} + \text{Dextrose} \rightarrow \text{Dihydroresorufin} + \text{gluconic acid} \quad \text{(Slowreaction)} \quad (4)$$

Note that the complete chemical formula of resazurin is 7-Hydroxy-3H-phenoxazin-3-one-10-oxide (molecular mass 229.19 g mol^{-1}).

A preliminary study (not detailed here) was carried out to define the best composition of catalyser (glucose and sodium hydroxide) in the dye solution, the one leading to:

- (quasi)-instantaneous kinetics for the oxidation of dihydroresorufin (colourless) into resorufin (pink),
- sufficiently slow kinetics (few minutes) for the reduction of resorufin (pink) into dihydroresorufin (colourless),
- high colourimetric yield (i.e. the colour intensity).

From this, the following formulation was chosen: glucose and sodium hydroxide were both diluted at 20 g L^{-1} in deionized water, and the concentration of resazurin was fixed at 0.1 g L^{-1}.

2.2. Description of the experimental set-up

The experimental set-up was the same as the one used by Roudet et al. (2011). It consisted of a straight horizontal channel of square cross section $A = l^2$ where $l = 2$ mm. The channel was carved

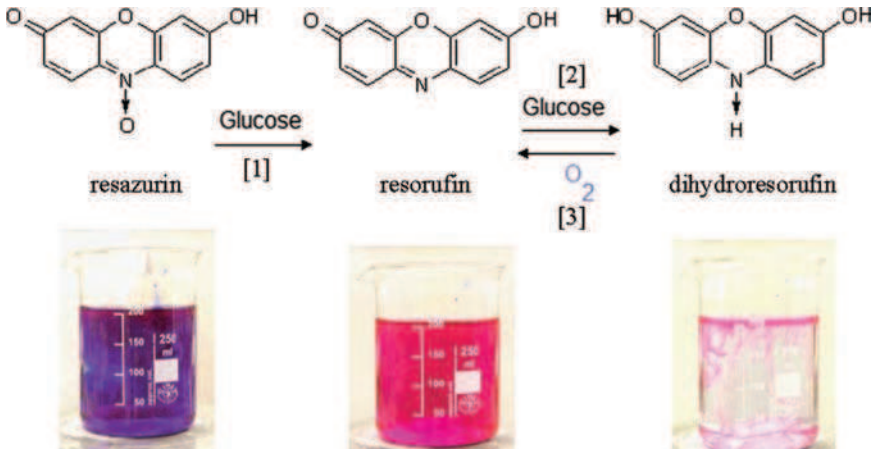

Fig. 1. Reduction of resazurin to resorufin by glucose and sodium hydroxide (step [1]). Reduction of resorufin to dihydroresorufin in presence of carbohydrate (step [2]). Reoxidation of dihydroresorufin to resorufin in presence of oxygen (step [3]). (For interpretation of the references to color in this figure legend, the reader is referred to the web version of this article.)

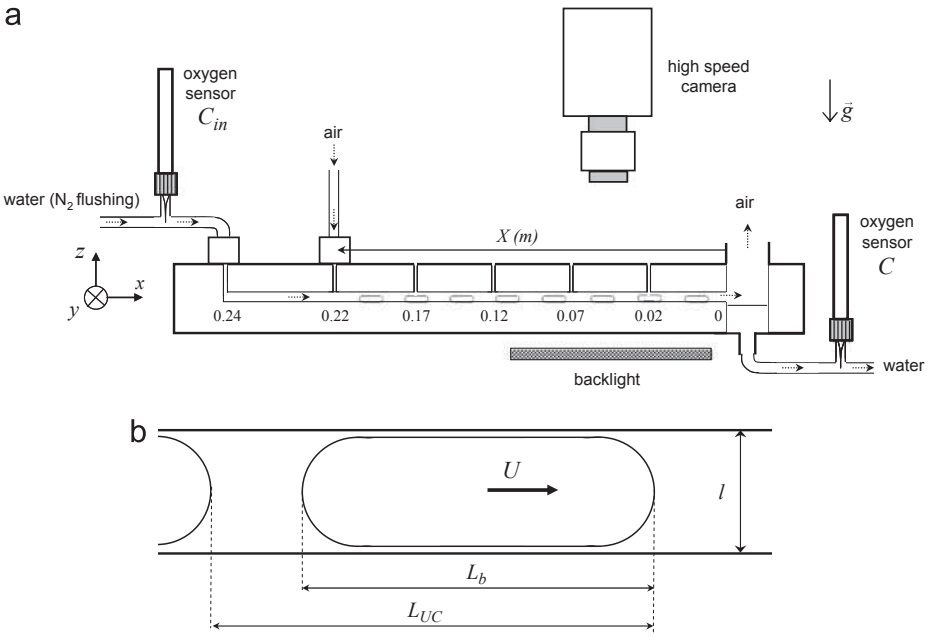

Fig. 2. (a) Experimental set-up for gas–liquid mass transfer measurements. (b) Schematic representation of two consecutive bubbles inside the channel (Unit Cell).

in a polymethyl methacrylate (PMMA) plate (0.03 m thick) and roofed over in a watertight manner by another plate (0.03 m thick).

Six holes 1.6 mm in diameter were pierced perpendicular to the channel in the carved plate at different distances from the exit. The liquid phase was injected at the first hole, located at $X=0.24$ m from the exit of the channel, and the gas phase at the second hole, located 0.02 m from the liquid phase injection point (Fig. 2a). Before entering the main channel, the gas phase (air) flowed through a winding of a 2-m-long capillary of 750 μm internal diameter. Gas and liquid were separated by gravity at the exit of the channel. The well in which the liquid flowed when leaving the channel was designed to ensure a stationary position of the liquid free surface under the channel exit.

Liquid flow rates Q_L were measured by a mass flow meter (Micro motion®); gas flow rates Q_G were controlled by a gas mass flow meter and mass flow controller (Brooks® model 5850E). Liquid flow rates ranged from 1 to 3 L h^{-1} and gas flow rates from 0.2 to 3 L h^{-1}. The associated superficial liquid and gas velocities were defined as $0.069 \leq j_L = Q_L/l^2 \leq 0.208$ m s^{-1} and $0.0139 \leq j_G = Q_G/l^2 \leq 0.208$ m s^{-1}.

2.3. Fluid properties

Experiments were performed at 293.15 K and atmospheric pressure. The fluids were air and deionized water containing D-glucose anhydrous (Fischer Scientific®, CAS 50-99-7), sodium hydroxide (VWR®, CAS 1310-73-2) and resazurin (Sigma Aldrich®, CAS 62758-13-8). The density (ρ_L), dynamic viscosity (μ_L) and static surface tension (σ_L) were measured by means of a pycnometer ($\rho_L \pm 0.2$ kg m^{-3}), a RM180 Rheomat Rheometric Scientific® viscometer ($\mu_L \pm 10^{-3}$ mPa s), and a Digidrop GBX® or Krüss tensiometer ($\sigma_L \pm 0.5$ mN m^{-1}), respectively. The oxygen saturation concentration, C^*, was measured by implementing the Winkler technique (Winkler, 1888) and by means of optical oxygen probes (Hach-Lange®). All the latter physicochemical properties are reported in Table 1. It can be observed that the colourimetric solution, with and without dye, had a surface tension, a viscosity and a density slightly higher than those of deionized water.

2.4. Image acquisition system for gas–liquid flow

The gas-liquid hydrodynamics inside the millimetric channel was investigated by a shadowgraph method. The channel was lit by a LitePad HO LED backlight (Rosco®) and bubbles were filmed with a monochromatic 10 bits high-speed camera (APX Photron) at 2000 frames per second. Image resolution is 20 μm per pixel The region of interest is 20 mm in length and 5 mm in width. The camera was positioned between $X=0.02$ and $X=0.07$ m from the exit of the channel (Fig. 2a). Image resolution was 20 μm per pixel. A dedicated image analysis algorithm was used to measure bubble length, L_b, bubble velocity, U, and distance between the noses of two consecutive bubbles, L_{UC}, (called the Unit Cell) (Fig. 2b). Bubble velocity U was deduced from the average displacements of the bubble nose between various time steps. These bubble characteristics were measured in presence of the colourimetric solution. The experimental errors associated with L_b, L_{UC} and U were found, respectively, equal to 0.05, 0.1 mm and 0.1 cm s^{-1}. They will be compared with the ones obtained by Roudet et al. (2011) in deionized water in Section 3 and in Table 2.

Table 1
Properties of deionized water and of the synthetic liquid media at 293.15 K.

Liquid phase	C (g L^{-1})	σ_L (mN m^{-1})	μ_L (mPa s)	ρ_L (kg m^{-3})	C^* (mg L^{-1})
Deionized water	0	71.4	1.003	996.8	9.05
Glucose	20	76	1.1176	1004.5	8.15
+NaOH	20				
Glucose	20	75	1.1176	1004.5	–
+NaOH	20				
+Resazurin	0.01				

Table 2
Bubble characteristics (measured in the colourimetric solution) versus liquid and gas flow rates.

Q_L (L h^{-1})	Q_G (L h^{-1})	L_b (mm)	L_{UC} (mm)	U (m s^{-1})	a (m^{-1})
1	0.2	2.22 (2.47)	12.67 (13.12)	0.098 (0.104)	275 (296)
	0.4	2.85 (3.00)	8.63 (8.82)	0.115 (0.121)	519 (534)
	0.6	3.05 (3.32)	6.10 (7.80)	0.137 (0.139)	785 (669)
	3	7.29 (7.85)	8.63 (9.65)	0.364 (0.360)	1326 (1278)
2	0.4	1.94 (2.00)	9.23 (9.90)	0.211 (0.219)	336 (317)
	0.6	2.30 (2.35)	6.77 (8.50)	0.228 (0.231)	533 (434)
	3	4.67 (4.85)	6.46 (6.92)	0.447 (0.445)	1137 (1101)
3	0.6	1.70 (n.d)	6.61 (n.d.)	0.321 (n.d)	464 (n.d.)
	1	1.78 (2.15)	5.68 (5.95)	0.335 (0.352)	493 (568)
	3	3.84 (3.67)	6.02 (5.77)	0.505 (0.534)	1002 (999)

The values measured by Roudet et al. (2011) in deionized water are reported into brackets.

2.5. Measurements of gas–liquid mass transfer

The transfer of oxygen from air bubbles into water was investigated over the range of gas and liquid flow rates defined in Section 2.1, which covers only the Taylor regime.

For each condition, images of the bubbles moving in the millimetric channel were recorded and digitally processed by a procedure developed within Matlab software (details in the next section). Note that, as the camera was monochromatic, the different levels of pink coloration taken by the dye solution (depending on the quantity of oxygen present) was represented by 253 grey levels on the acquired images. The recording time between two images was equal to 0.5×10^{-3} s.

The results obtained with this colourimetric method were compared with those determined by Roudet et al. (2011) in the same channel. These authors measured the volumetric gas–liquid mass transfer coefficients, k_La, by means of two oxygen microsensors (Unisense® OX500, 400–600 μm in tip diameter) located a few centimetres before the entrance and after the exit of the channel.

3. Implementation of the colourimetric technique

3.1. Image processing

Let $GV(x,y,t)$ be the grey level of a pixel with coordinates x, y of an untreated raw image at time t. As shown in Fig. 3a, this grey level is darkest at the bubble surface and lightest in the region free of oxygen, the intermediate grey levels being linked to the different coloured forms taken by the dye solution in presence of oxygen. The purpose of the present section is to extract an accurate quantification of the oxygen transferred from the raw images. For this purpose, an image processing technique had to be developed, which mainly identified the boundaries demarcating these three ranges of grey levels.

The first step was the characterization of the “lightest” region mentioned above, a zone without bubbles or mass transfer. For all experiments, the positions of the camera, LitePad backlight and channel remained unchanged and there was no alteration of the “uncoloured” form of the dye. Consequently, the grey levels corresponding to this “no-transfer zone” should theoretically remain constant from one recorded image to another. In practice,

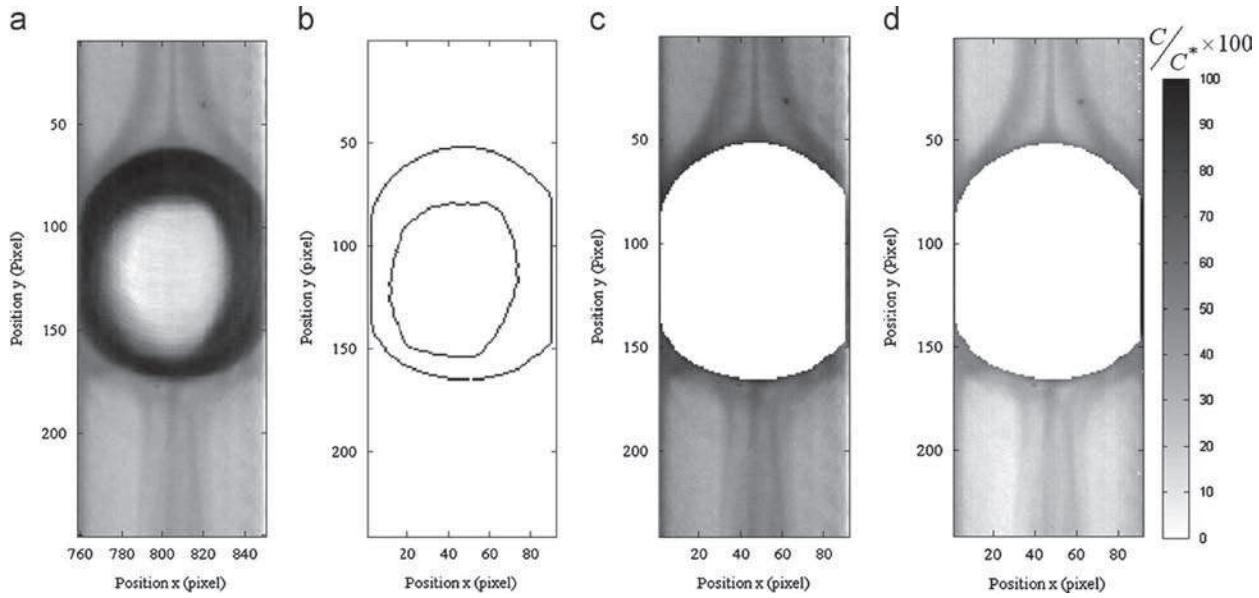

Fig. 3. Image processing (a) raw image (b) detection of the bubble contour (c) corrected image after subtracting the contribution of background and noise, and masking the bubble (d) Equivalent oxygen concentration field obtained after applying the calibration curve. The experiments were conducted with a concentration of resazurin of 0.1 g L^{-1}.

a variation of less than 3 grey levels was observed in this zone over the whole set of recorded images. Based on this observation, a reference image, determined by averaging 50 images without bubbles, was considered and subtracted from the raw images. The average grey level of the corrected image background thus became close to 0. Note that (i) this subtraction was also a means of correcting the spatial non-homogeneity of the lighting, (ii) the choice of the number of images (here 50) was validated by convergence tests on the cumulative average. Nevertheless, as there was some temporal non-homogeneity in the lighting, the mean value of the background grey level could still be different from 0 or vary between two successive images. It was imperative to correct this defect since it led to some distortions in the corresponding oxygen concentration fields. For this correction (i.e. to ensure a background at a null mean value for all the recorded images), the histogram of grey levels of each image was determined. Whatever the image, the histogram was characterized by an almost Gaussian shape, with a known mean and standard deviation. Based on that, the histogram mean value was subtracted from each grey level of the recorded image. In this way, the mean value of the background grey level was shifted to 0 and thus the non-homogeneities of the lighting could be satisfactorily corrected.

From the resulting image, a threshold was fixed to determine the boundary between mass transfer and noise. Then, all the grey levels lighter than this threshold were considered as noise and set to 0. This threshold is chosen in such a way that the remaining noise is minimized while ensuring that the mass transfer is not disrupted. It has been found that twice the standard deviation is the optimal threshold for the most considered cases. Then, all the pixels whose grey level is below this threshold are considered as noise and their value is set to 0. The following step of the image processing concerned the second extreme values of grey levels, namely the "darkest" ones, corresponding to the bubble surface. The Canny edge detector algorithm (extracted from the Image Processing ToolBox in Matlab®), was used to determine the bubble contours. It is mainly based on the location of local maximum gradients of grey levels for a given image, to which a Gaussian filter has previously been applied to reduce the noise level. The larger the gradient is, the more likely it is that the pixel represents an edge. Then a thresholding procedure with hysteresis is considered to determine whether the pixel is an edge or not. For further details about this method, the reader is invited to consult Canny (1986). An example of edge detection using the Canny detector is shown in Fig. 3b. It can be observed that two circular edges have been detected: the largest one describes the global shape of the bubble and enables the bubble diameter to be determined, whereas the second edge is due to the bubble part in contact with the square channel and under a strong light due to the backlight positioned behind the recorded bubble. Finally, to cancel this rear reflect, each pixel belonging to the largest detected edge is considered as belonging to the bubble and its corresponding grey value is then set to 0. Fig. 3c represents the corrected image after application of the bubble mask. The grey level of the corrected image is noted $GV^*(x,y,t)$.

Thanks to this image processing, the pixels on the final corrected image which had non null values of grey levels could be directly attributed to the quantity of oxygen transferred per unit of liquid volume. By considering a pixel-by-pixel summation on the remaining grey levels and applying the calibration curve mentioned above, an accurate quantification of the oxygen transferred by bubbles was possible (see Fig. 3d).

3.2. Calibration curve

A calibration curve had to be established to convert the grey level into equivalent oxygen concentration fields. The term "equivalent" refers here to the fact the real dissolved oxygen concentrations are null in the present experiments as the quantity of oxygen transferred per unit of liquid volume entirely reacts with the dye. To avoid any confusion, we will thereafter note C this equivalent oxygen concentration, which, rigorously speaking, corresponds to quantity of oxygen transferred per unit of liquid volume.

For this, several colourimetric solutions were prepared at different concentrations of resazurin (0.05 and 0.01 g L^{-1}). They were saturated in oxygen with air in order to reach their highest intensity of pink (or their highest value of grey level on the acquired image). For each colourimetric solution flowing in the channel (without bubbles), about 50 pictures were recorded and

averaged. In addition, images were acquired when no oxygen was present in the colourimetric solution. The third averaged images obtained showed how the grey level changed according to the resazurin concentration (Fig. 4a).

The stoechiometry of the reaction between oxygen and dihydroresorufin is given by Eq. (3). Then, the number of moles of dissolved oxygen can easily be deduced from the number of moles of resazurin, as

$$n_{O_2\text{transferred}} = n_{O_2\text{reacted}} = \frac{n_{\text{dihydroresorufin}}}{2} = \frac{n_{\text{resazurin}}}{2} \quad (5)$$

Thus, for each resazurin concentration (0, 0.05 and 0.1 g L^{-1}), it is possible to associate the measured averaged grey level with an equivalent oxygen concentration C. The calibration curve obtained is plotted in Fig. 4b. The perfect linearity observed between grey level and the quantity of oxygen transferred per unit of liquid volume is remarkable and is an undeniable advantage of this method, especially when compared to the PLIFI technique. It is also important to note that this calibration curve is attached to the present experimental set-up and conditions. In other words, if a change is made in the light or camera parameters, the calibration has to be performed again.

Using the calibration curve, the equivalent oxygen concentration $C(x,y,t)$ can be calculated for each corrected grey level $GV^*(x,y,t)$, as shown in Fig. 3d. The main drawback of this procedure is that, if a pixel in the corrected image has a grey level higher than the one corresponding to the calibration limit (here an equivalent oxygen concentration of 13 mg L^{-1}), the conversion of the grey level into equivalent oxygen concentration field is not possible.

4. Results

Some corrected images of gas–liquid flows are shown in Fig. 5 for different operating conditions corresponding to the Taylor flow regime. They were obtained by implementing the image processing and the calibration procedure described in Section 3. They clearly illustrate how the equivalent oxygen field in the liquid phase changes with the bubble lengths and distances between two consecutive bubbles. Note that the bubbles stability, and consequently of the oxygen fields, in time was verified.

As observed by Roudet et al. (2011), the corresponding bubble Reynolds numbers Re (defined using the bubble velocity U) range from 200 to 1500, indicating that the inertial effects are important in the liquid phase and contribute largely to the deformation of bubbles. In fact, when the numbers controlling the bubble shape are compared, the inertial effects are clearly dominant with respect to viscosity and gravity effects: the Weber numbers We

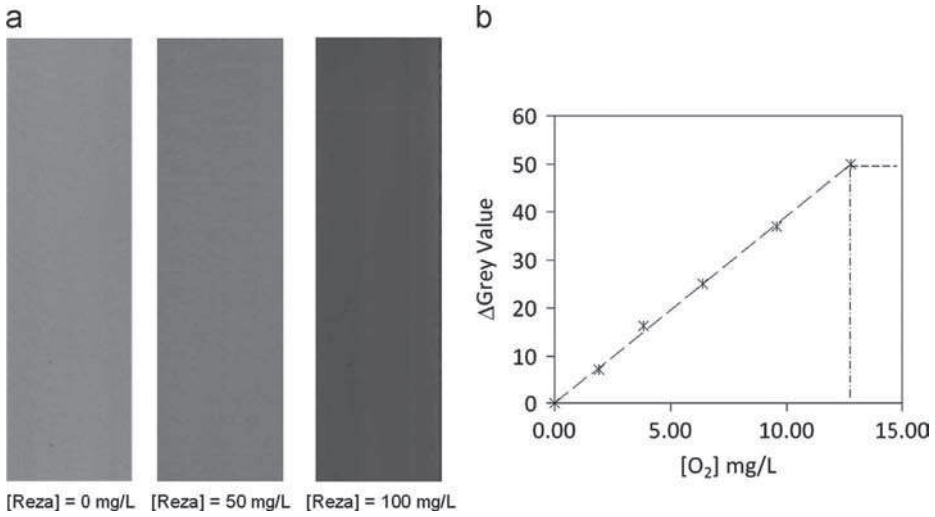

Fig. 4. (a) Variation of the grey level in the millichannel for different resazurin concentrations (b) calibration curve between grey level and quantity of oxygen transferred per unit of liquid volume. (For interpretation of the references to color in this figure legend, the reader is referred to the web version of this article.)

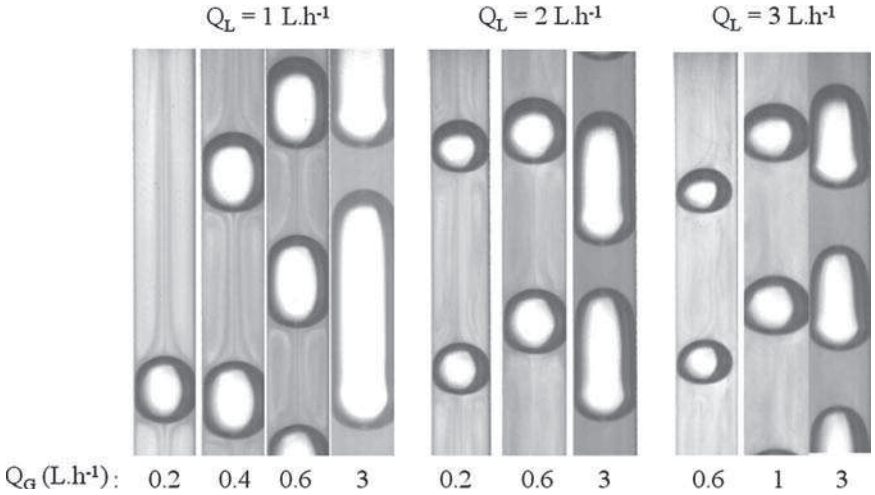

Fig. 5. Equivalent oxygen concentration fields for several hydrodynamic conditions.

are higher than the capillary numbers *Ca* and the Bond number *Bo*, except for $Re < 250$ where inertial and gravity effects have the same order of magnitude.

Data for bubble velocity U, bubble length L_b and unit cell length L_{UC} (Fig. 2b) are reported in Table 2 for the operating conditions investigated. They were measured in the oxygen-sensitive dye solution. A comparison with those obtained by Roudet et al. (2011) shows little deviation (5% on average), thus demonstrating that, when some experimental uncertainties and the possible alteration of the channel surface with time are taken into account, the effect of the physicochemical properties of the colourimetric solution on the bubble characteristics (Table 1) is negligible.

From Fig. 5, it can first be observed that the equivalent oxygen concentration is the strongest in the wake and in front of the bubbles, as well as near the channel walls. This can be explained by the well-known structure of such gas–liquid flows, first postulated by Taylor (1961):

- the film between the bubble and the channel wall moves in the opposite direction to the bubble.
- the wake of the bubble is characterized by some vortices generated by the positive wake of the bubble and the thin layer of liquid moving in the other direction. In the frame of reference of the bubble, this is described by stagnation points at the bubble nose and tail, which cause flow reversal and create a recirculation motion along the length of the liquid slug.

This behaviour is confirmed by the visualization of mass transfer proposed in Figs. 5 and 6.

Fig. 6 shows an example of 2D and 3D graphical representations of the quantity of oxygen transferred per unit of liquid volume around a bubble. We can observe that:

- in the wall part, the concentration appears higher and close to the maximum saturation concentration. However, the associated values should be taken with caution as, in this zone, the light reflected from the wall surface could induce an artificial increase in pink colour intensity (and so in grey level on the raw images), and thus bias the accuracy of the measurement.
- in the liquid slug zone, the equivalent oxygen concentration seems lower at the bottom of the bubble than in the front of the bubble. One explanation of this dissymmetry could be that the steady state had not been reached for oxygen transfer due to a short length channel (0.22 m) or to the formation of the bubble.

For different hydrodynamic conditions, a comparison of the equivalent oxygen fields is proposed in Fig. 7. When the liquid slug

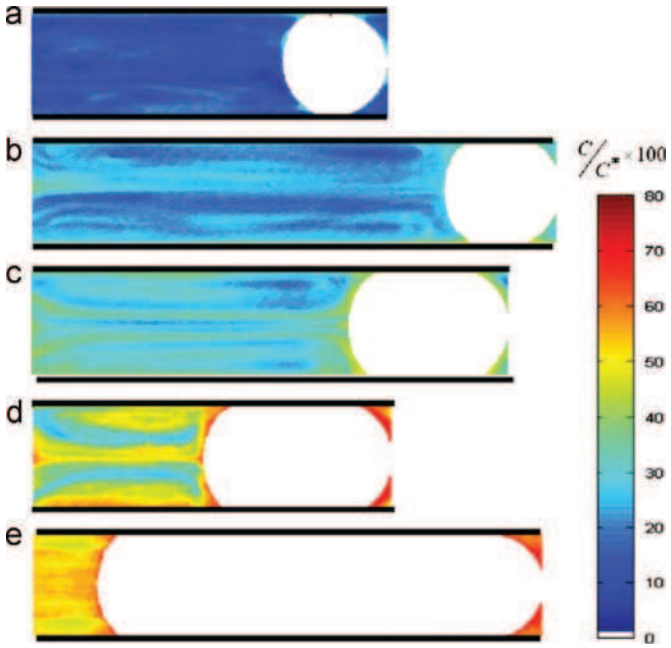

Fig. 7. Comparison between different hydrodynamic conditions of equivalent oxygen concentration fields: (a) $Q_G = 0.6\ L\ h^{-1}$, $Q_L = 3\ L\ h^{-1}$; (b) $Q_G = 0.2\ L\ h^{-1}$, $Q_L = 1\ L\ h^{-1}$; (c) $Q_G = 0.4\ L\ h^{-1}$, $Q_L = 1\ L\ h^{-1}$;(d) $Q_G = 0.6\ L\ h^{-1}$, $Q_L = 1\ L\ h^{-1}$; (e) $Q_G = 3\ L\ h^{-1}$, $Q_L = 1\ L\ h^{-1}$;

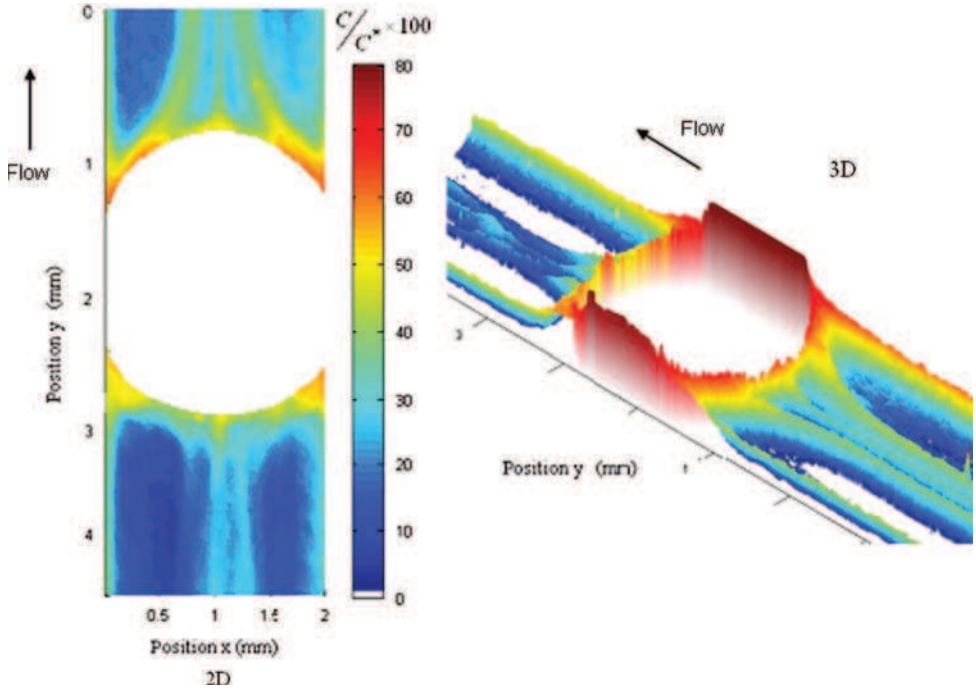

Fig. 6. Equivalent oxygen concentration field around a moving bubble for $Q_L = 1\ L\ h^{-1}$ and $Q_G = 0.2\ L\ h^{-1}$

volumes decrease (i.e. the bubble lengths increase), the equivalent oxygen concentration level is greater in the bubble wake; the concentration in the bubble wake is almost zero in the first sequence (Fig. 7a), for which the contact time between gas and liquid is small, 1.5 mg L^{-1} for Fig. 7b, 2.46 mg L^{-1} for Fig. 7c, 3.63 mg L^{-1} for Fig. 7d and 5.23 mg L^{-1} for Fig. 7e.

We can also logically observe that an increase in gas flow rate leads to a rise in the quantity of oxygen transferred per unit of liquid volume and the effect is opposite for increasing liquid flow rates.

As is it possible to quantify the quantity of oxygen transferred per unit of liquid volume in the liquid phase and in the liquid film; a calculation technique can be developed to estimate the mass transfer coefficient, as shown in the next section.

5. Discussion

The purpose of this section is to evaluate, from the equivalent oxygen concentration fields presented above, the liquid-side mass transfer coefficient (k_L).

As established by Roudet et al. (2011), the volumetric mass flux of oxygen from gas to liquid along the channel can be expressed as:

$$\varphi(X') = j_L \times \frac{\partial \overline{C_{\mathrm{mes}}}}{\partial X'} \tag{6}$$

where X' is the axial position in the channel such that $X'=0$ at the location where the bubbles are generated (corresponding to $X=0.22$ m in Roudet et al., 2011) and $X'=0.22$ m at the exit of the channel. $\overline{C}_{\mathrm{mes}}$ is the average equivalent oxygen concentration accumulated in the liquid phase at the axial position X' along the channel: it corresponds to the quantity of oxygen transferred in the liquid phase per unit of liquid volume which reacted with the dye.

Assuming that the real concentration of dissolved oxygen in the liquid at the scale of the unit cell is zero due to its consumption by the chemical reaction, the mass flux of oxygen (per unit of liquid volume) can be also expressed by:

$$\varphi(X') = k_L \times a \times C^* \tag{7}$$

where k_L is the liquid-side mass transfer coefficient and a the interfacial area between gas and liquid phases. The latter assumption was validated using an oxygen microsensor (Unisense® OX500, 400–600 μm in tip diameter): during all experiments, the signal of the sensor, which represents the mean value of dissolved oxygen concentration at the exit of the channel, remained null.

By coupling Eqs. (6) and (7), the usual relationship, based on a plug flow model in liquid phase, is found:

$$\frac{\partial \overline{C_{\mathrm{mes}}}}{\partial X'} = \frac{k_L \times a \times C^*}{j_L} \tag{8}$$

Neglecting the oxygen transferred at the bubble formation, integrating Eq. (8) on a unit cell gives:

$$\overline{C_{\mathrm{mes}}} = \frac{k_L \times a \times X' \times C^*}{j_L} \tag{9}$$

In order to estimate the interfacial area, a, between the gas and liquid phases in a unit cell, a hemispherical shape is assumed for the bubble nose and rear, with a cylindrical shape for the bubble body. This is true only in the Taylor regime. With these assumptions, the specific interfacial area for the liquid film a_f and the recirculating region a_r are given by

$$a_f = \frac{\pi \times l \times (L_b - l)}{L_{UC} \times l^2} = \frac{\pi \times (L_b - l)}{L_{UC} \times l} \tag{10}$$

$$a_r = \frac{2(\pi \times l^2/2)}{L_{UC} \times l^2} = \frac{\pi}{L_{UC}} \tag{11}$$

The total interfacial area, a, is the sum of the two specific areas ($a=a_f+a_r$) and can be calculated from the data reported in Table 2.

The oxygen transferred by a single bubble can then be tracked by the equivalent oxygen accumulation in the unit cell, as

$$\overline{C_{\mathrm{mes}}} = \frac{\iint C_{\mathrm{mes}}(x,y) \times dx \times dy \times dz}{L_{UC} \times l^2} \tag{12}$$

Eq. (12) does not take the dimension z related to the channel height into account for integrating C_{mes}. This is because the present colourimetric technique is not able to visualize (and thus to discriminate) the equivalent oxygen concentration fields related to each xy-planes along the channel height. Consequently, we should keep in mind that the equivalent oxygen concentration obtained at a given location (x,y) is a mean value along the z-axis. Moreover, as the bubble nose and rear have a hemispheric shape, the liquid volume associated to these bubble areas cannot be visualised and then is not taken account for the calculation. This leads to a maximum error of 13% on the volume estimation of the unit cell.

Finally, from Eqs. (9) and (12), the liquid-side mass transfer coefficient can be calculated as:

$$k_L = \frac{\overline{C}_{\mathrm{mes}} \times j_L}{X' \times a \times C^*} \tag{13}$$

The variation of k_L with gas flow rate is plotted in Fig. 8a (the associated numerical values being reported in Table 3). It can be observed that: (i) for a given value of Q_G, k_L increases with increasing Q_L, (ii) for a fixed value of Q_L, k_L decreases when Q_G increases. Fig. 8b shows that the volumetric mass flux of oxygen increases with increasing bubble lengths. This is in agreement with Fig. 7, in which the equivalent oxygen concentration in the recirculation loop between two consecutive bubbles almost reaches the saturation concentration for large bubbles. The order of magnitude of the interfacial area, a, goes from 250 to 1200 m^2 m^{-3}. As expected (Yue et al., 2007), the values of a are significantly higher than in usual gas–liquid macro-contactors, almost the same as in static mixers and smaller than in micro-channels. All these findings are in agreement with the results reported in the literature in which chemical or physical methods are involved.

In order to validate the colourimetric technique, the liquid-side mass transfer coefficients above should be compared to those obtained in the literature (Table 3). The main difficulty is that this type of experimental data is not available for experiments performed in presence of glucose solution. By default, we have compared with the results of Roudet et al. (2011) obtained in the same channel but with deionized water. As shown in Table 3, rather good agreement is observed with a mean standard deviation of about 20%. These differences can probably be attributed to the changes in physicochemical properties, as already mentioned (Table 1). In addition, some measurements using the same methodology as Roudet et al. (2011) (namely using oxygen probes) were performed in the colourimetric solution without resasurin (to avoid the chemical reaction which entirely consumes the dissolved oxygen); the associated results are reported in the last column of Table 3. They lead to a better agreement (the standard deviation falls to 9%), confirming the potential effect of liquid phase properties. So, these two comparisons enable us to validate the use of the colourimetric technique as a tool for measuring liquid-side mass transfer coefficients. Nevertheless, we should bear in mind that all the values of k_L presented depend closely on the calculation of the interfacial area, which is based on specific

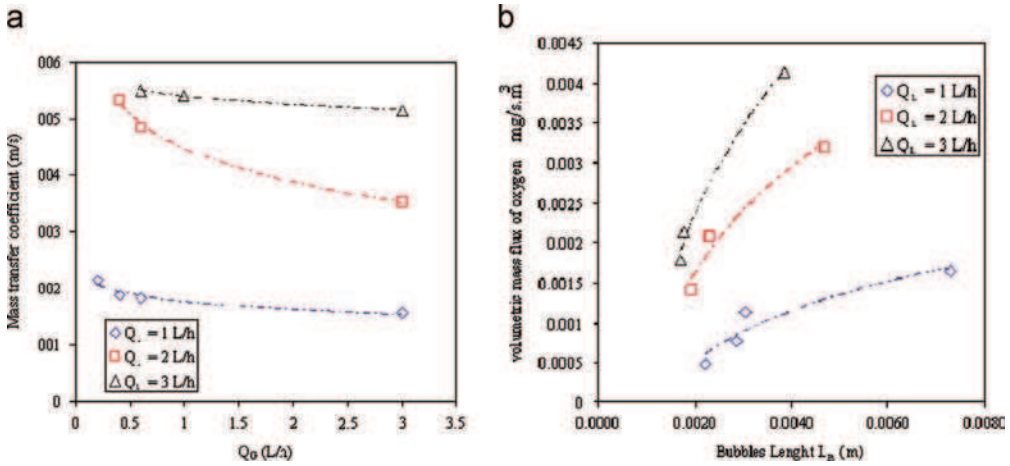

Fig. 8. Liquid-side mass transfer coefficient versus gas flow rate (b) volumetric mass flux of oxygen transferred in the liquid versus bubble length.

Table 3
Comparison of liquid-side mass transfer coefficient obtained by the colourimetric technique and by a classic probe technique (Roudet et al., 2011).

Liquid flow rate Q_L ($L\,h^{-1}$)	Gas flow rate Q_G ($L\,h^{-1}$)	Liquid-side mass transfer coefficient k_L ($m\ s^{-1}$)		
		Colourimetric method using oxygen concentration fields	Roudet et al. (2011) (Deionized water)	Probe measurement (colourimetric solution without dye)
1	0.2	2.14×10^{-4}	1.43×10^{-4}	2.36×10^{-4}
	0.4	1.86×10^{-4}	–	–
	0.6	1.81×10^{-4}	1.37×10^{-4}	–
	3	1.55×10^{-4}	1.71×10^{-4}	1.40×10^{-4}
2	0.4	5.33×10^{-4}	–	–
	0.6	4.86×10^{-4}	3.20×10^{-4}	–
	3	3.52×10^{-4}	3.70×10^{-4}	3.96×10^{-4}
3	0.6	5.49×10^{-4}	–	–
	1	5.41×10^{-4}	–	–
	3	5.15×10^{-4}	4.27×10^{-4}	5.49×10^{-4}

assumptions on the bubble shape and on a 2D integration of contribution field.

Thanks to the equivalent oxygen concentration field, it is also possible to separate the contributions of the wall film and the recirculating region. The associated liquid-side mass transfer coefficients, $k_{L,f}$ and $k_{L,r}$, are then expressed as:

$$k_{L,f} = \frac{\overline{C_f} \times j_L}{X' \times a_f \times C^*} \tag{14}$$

$$k_{L,r} = \frac{\overline{C_r} \times j_L}{X' \times a_r \times C^*} \tag{15}$$

where $\overline{C_f}$ and $\overline{C_r}$ are the average equivalent oxygen concentrations accumulated, in the wall film and in the recirculating region, respectively, at axial position X' along the channel. They are calculated from Eq. (12), but by considering only the points (x,y) belonging to the wall film or to the recirculation region inside a unit cell (we have adopted the same definitions for these regions as Roudet et al. (2011)).

Fig. 9a represents the ratio between the local (i.e. in the wall film or in the recirculating zone) and the global (deduced from Eq. (13)) liquid-side mass transfer coefficients k_L versus bubble length.

It can be observed that, for the recirculation region, the local mass transfer coefficient, $k_{L,r}$, increases with increasing bubble lengths until it reaches a plateau close to 1 ($k_{L,r} \approx k_L$). In contrast, the local mass transfer coefficient associated with the film region never achieves this constant value. This is consistent with previous observations concerning the length of the present millimetric channel, which is not enough long to saturate the film region. The equivalent oxygen concentration in this wall region starts from 6 to 7 $mg\,L^{-1}$ for the smallest bubbles, and falls to only 2 $mg\,L^{-1}$ for the biggest bubbles. This clearly confirms the findings of Roudet et al. (2011), namely that the length of the channel should be increased to improve the mass transfer efficiency. A more important point is that this colourimetric visualization technique offers the undeniable advantage (especially for milli-reactor design) of being able to evaluate the saturation of the film.

We now compare the previous experimental liquid-side mass transfer coefficient with the ones predicted by the fundamental model developed by Van Baten and Krishna (2004). These authors proposed to calculate liquid-side mass transfer coefficients from Higbie's penetration theory as:

$$k_L = 2\sqrt{\frac{D}{\pi \times t_C}} \tag{16}$$

where t_c is the contact time between gas and liquid that can be expressed for both regions and D the diffusion coefficient. For the latter parameter, the value measured by Jimenez et al. (2013) in the same liquid medium have been considered, namely $D = 1.50 \times 10^{-9}\ m^2\ s^{-1}$.

In the liquid film area, it is defined by:

$$t_{cf} = \frac{L_b - l}{U} \tag{17}$$

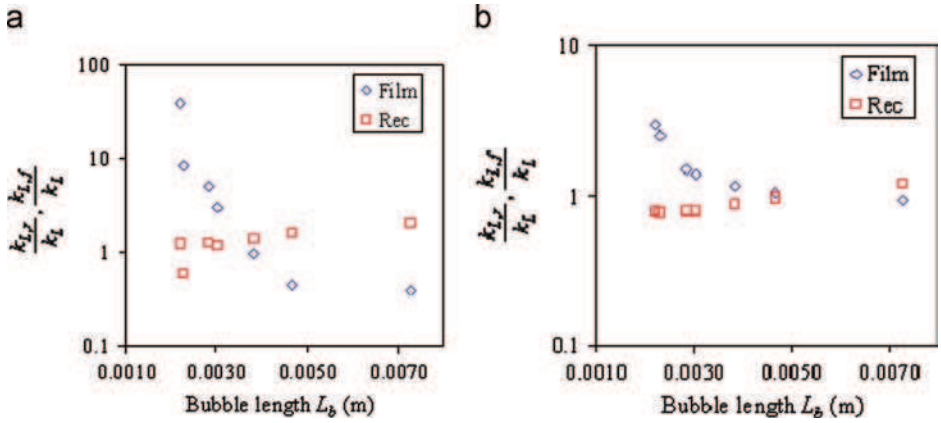

Fig. 9. Ratio between local and global mass transfer coefficients as a function of bubble length (a) experimental (b) Van Batten model.

and in the recirculating region by

$$t_{cr} = \frac{\pi \times l/2}{U} = \frac{\pi \times l}{2U} \tag{18}$$

Then, we obtain:

$$k_{l,r} = 2\sqrt{\frac{D}{\pi \times t_{cr}}} = 2\sqrt{\frac{D}{\pi \times (\pi \times l/2U)}} = \frac{2\sqrt{2}}{\pi}\sqrt{\frac{D \times U}{l}} \tag{19}$$

$$k_{l,f} = 2\sqrt{\frac{D}{\pi \times t_{cf}}} = 2\sqrt{\frac{D}{\pi \times (L_b - l/U)}} = \frac{2}{\sqrt{\pi}}\sqrt{\frac{D \times U}{(L_b - l)}} \tag{20}$$

Fig. 9b represents the ratio between the theoretical local (i.e. in the wall film or in the recirculating zone) and the experimental global liquid-side mass transfer coefficients k_L as a function of bubble length. Compared to the experimental ratios, the model provides the right orders of magnitude for the liquid-side mass transfer coefficient, and trends similar to experimental data. Nevertheless, the model clearly provides underestimates relative to experiments. This could be explained by the facts that: (i) the mass transfer occurring during the bubble formation stage is not taken into account in the model, (ii) some experimental uncertainties clearly exist in the measurement of the equivalent oxygen concentration at the wall of the channel.

6. Conclusion

The implementation of a colourimetric technique to measure equivalent oxygen concentration fields has been presented. This technique is based on the reaction of oxygen molecules, in presence of an alkaline solution, with a dye, the colour of which changes depending on whether it is in reduced or oxidized form. A digital treatment of the raw images was suggested for deducing the fields representing the local quantity of oxygen transferred per unit of liquid volume (acquisition of reference images, background noise images). A calibration was established to link the variation in grey level of the corrected images with the equivalent oxygen concentration (contrary to the PLIF technique, a linear relationship was observed between grey level and oxygen concentration).

This technique was applied to the gas–liquid mass transfer occurring when air bubbles flow in a millimetric square channel. For various hydrodynamic conditions, the equivalent oxygen concentration fields were compared and, from them, the liquid-side mass transfer coefficients were calculated. It was also possible to separate the contributions of the wall film and of the recirculating region.

This study thus constitutes a striking example showing that this new colourimetric method (easy to implement as without laser source) could be an interesting tool for investigating gas–liquid mass transfer in transparent fluids. This information gives new insight into the complex mechanism of gas–liquid mass transfer in millimetric channels and could help to develop rigorous theoretical models and numerical simulations. Nevertheless, as at present implemented (i.e. concentration fields averaged along the *z*-axis), this technique remains useful preferentially for 2D or pseudo-2D flows. In the future, various improvements will be performed to overcome some current technical limitations, such as the use of a second camera to acquire the grey level maps along the *z*-axis (in particular for visualizing what happens in the areas around the hemispheric rear and nose of the bubbles, and for appreciating the axisymmetrical character of the concentration fields).

Nomenclature

α	specific interfacial area (m^{-1})
A	channel cross-sectional area (m^2)
C	equivalent oxygen concentration (or riourously speaking, the quantity of oxygen transferred in the liquid phase per unit of liquid volume) (kg m^{-3})
$\overline{C}_{mes}$	average equivalent oxygen concentration accumulated in the liquid phase at the axial position X' along the channel calculated (deduced from calculations) (kg m^{-3})
C^*	dissolved oxygen concentration at saturation (kg m^3)
D	diffusion coefficient of oxygen in the liquid phase (m^2 s^{-1})
g	gravity acceleration (m s^{-2})
j_G	gas superficial velocity (m s^{-1})
j_L	liquid superficial velocity (m s^{-1})
k_L	liquid-side mass transfer coefficient (m s^{-1})
k_La	volumetric gas–liquid mass transfer coefficient (s^{-1})
l	width of the channel (m)
L_b	length of the bubble (m)
L_{UC}	length of the unit cell (m)
Q_G	gas volumetric flow rate (m^3 s^{-1})
Q_L	liquid volumetric flow rate (m^3 s^{-1})
t	time (s)
U	bubble velocity (m s^{-1})
X	location of gas injection from the exit of the channel (m)

Greek letters

δ	liquid film thickness (m)
φ	mass flux of oxygen in the liquid per unit of liquid volume (kg s^{-1} m^{-3})
μ_L	dynamic viscosity (Pa s)

ρ_L	density (kg m^{-3})
σ	surface tension (N m^{-1})
τ	residence time for the liquid phase (s)

Dimensionless numbers

Bo	Bond number ($Bo = (\rho_L \times g \times l^2/\sigma)$)
Ca	Capillary number ($Ca = (\mu_L \times U/\sigma)$)
Re	Reynolds number ($Re = (\rho_L \times U \times l/\mu_L) = (We/Ca)$)
We	Weber number ($We = (\rho_L \times U^2 \times l/\sigma)$)

Acknowledgement

The authors would like to thank Emanuel Cid and Pr. Anne-Marie Billet from the *Laboratoire de Génie Chimique* of Toulouse for the fruitful discussions that took place around this work.

References

Aoki, N., Tanigawa, S., Mae, K., 2011. A new index for precise design and advanced operation of mass transfer in slug flow. Chem. Eng. J. 167, 651–656.

Banerjee, S., Scott, D.S., Rhodes, E., 1970. Studies in cocurrent gas–liquid flow in helically coiled tubes. Part 11: theory and experiments on turbulent mass transfer with and without chemical reaction. Can. J. Chem. Eng. 48, 542–551.

Barnea, D., Luninski, Y., Taitel, Y., 1983. Flow pattern in horizontal and vertical two-phase flow in small diameter pipes. Can. J. Chem. Eng. 61, 617–620.

Bercic, G., Pintar, A., 1997. The role of gas bubbles and liquid slug lengths on mass transport in the Taylor flow through capillaries. Chem. Eng. Sci. 52 (21,22), 3709–3719.

Canny, J., 1986. A computational approach to edge detection. IEEE Trans. Pattern Anal. Mach. Intell. 8, 679–698.

Cook, A.G., Tolliver, R.M., Williams, J.E., 1994. The blue bottle experiment revisited gives some details of the reaction mechanism and alternative dyes. J. Chem. Educ. 71, 160, http://dx.doi.org/10.1021/ed071p160.

Engerer, S.C, Gilbert Cook, A., 1999. The blue bottle reaction as a general chemistry experiment on reaction mechanisms. J. Chem. Educ. 76 (11), 1519, http://dx.doi.org/10.1021/ed076p1519.

François, J., Dietrich, N., Guiraud, P., Cockx, A., 2011. Direct measurement of mass transfer around a single bubble by micro-PLIFI. Chem. Eng. Sci. 66, 3328–3338.

Fries, D.M., Trachsel, F., von Rohr, P.R., 2008. Segmented gas–liquid flow characterization in rectangular microchannels. Int. J. Multiphase Flow 34, 1108–1118.

Gunther, A., Khan, S.A., Thalmann, M., Trachsel, F., Jensen, K.F., 2004. Transport and reaction in microscale segmented gas–liquid flow. Lab Chip, 278–286.

Gupta, R., Fletcher, D.F., Haynes, B.S., 2010. Taylor flow in microchannels: a review of experimental and computational work. J. Comput. Multiphase Flows 2 (1), 1–31.

Higbie, R., 1935. The rate of absorption of a pure gas into a still liquid during short periods of exposure. Trans. A.I.Ch.E 31, 365–389.

Jimenez, M., Dietrich, N., Cockx, A., Hébrard, G., 2013. Experimental study of O_2 diffusion coefficient measurement at a planar gas–liquid interface by planar laser-induced fluorescence with inhibition. AIChE J. 59 (1), 325–333.

Kreutzer, M.T., Kapteijn, F., Moulijn, J.A., Heiszwolf, J.J., 2005. Multiphase monolith reactors: chemical reaction engineering of segmented flowing microchannels. Chem. Eng. Sci. 60, 5895–5916.

O'Brien, J., Wilson, I., Orton, T., Pognan, F., 2000. Investigation of the Alamar Blue (resazurin) fluorescent dye for the assessment of mammalian cell cytotoxicity. Eur. J. Biochem. 267, 5421–5426.

Roudet, M., Loubière, K., Gourdon, C., Cabassud, M., 2011. Hydrodynamics and mass transfer in inertial gas–liquid flow regimes through straight and meandering millimetric square channels. Chem. Eng. Sci 66, 2974–2990.

Shao, N., Gavriilidis, A., Angeli, P., 2009. Flow regimes for adiabatic gas–liquid flow in microchannels. Chem. Eng. Sci. 64, 2749–2761.

Sobieszuk, P., Cyganski, P., Pohorecki, R., 2008. Volumetric liquid side mass transfer coefficient in a gas–liquid microreactor. Chem. Proc. Eng. 29, 651–661.

Sobieszuk, P., Pohorecki, R., Cyganski, P., Grzelka, J., 2011. Determination of the interfacial area and mass transfer coefficients in the Taylor gas–liquid flow in a microchannel. Chem. Eng. Sci. 66 (23), 6048–6056.

Sobieszuk, P., Aubin, J., Pohorecki, R., 2012. Hydrodynamics and mass transfer in gas–liquid flows in microreactors. Chem. Eng. Technol. 35 (8), 1346–1358.

Su, H., Wang, S., Niu, H., Pan, L., Wang, A., Hu, Y., 2010. Mass transfer characteristics of H2S absorption from gaseous mixture into methyldiethanolamine solution in a T-junction microchannel. Sep. Purif. Technol. 72 (3), 326–334.

Taha, T., Cui, Z.F., 2006. CFD modelling of slug flow inside square capillaries. Chem. Eng. Sci. 61, 665–675.

Tan, J., Lu, Y.C., Xu, J.H., Luo, G.S., 2012. Mass transfer performance of gas–liquid segmented flow in microchannels. Chem. Eng. J., 181–182229–2353.

Taylor, GI, 1961. Deposition of a viscous fluid on the wall of a tube. J. Fluid Mech. 10 (2), 161–165.

Thulasidas, T.C., Abraham, M.A., Cerro, R.L., 1997. Flow patterns in liquid slugs during bubble-train flow inside capillaries. Chem. Eng. Sci. 52 (17), 2947–2962.

Van Baten, J.M., Krishna, R., 2004. CFD simulations of mass transfer from Taylor bubbles rising in circular capillaries. Chem. Eng. Sci. 59, 2535–2545.

Vandu, C.O., Liu, H., Krishna, R., 2005. Mass transfer from Taylor bubbles rising in single capillaries. Chem. Eng. Sci. 60, 6430–6437.

Yue, J., Chen, G., Yuan, Q., Luo, L., Gonthier, Y., 2007. Hydrodynamics and mass transfer characteristics in gas–liquid flow through a rectangular microchannel. Chem. Eng. Sci. 62, 2096–2108.

Walter, R., Vandaveer, I.V., Mosher, Mel, 1997. The blue bottle revisited. J. Chem. Educ. 74 (4), 402, http://dx.doi.org/10.1021/ed074p402.

Wellman, W.E., Noble, M.A., 2003. Greening the blue bottle. J. Chem. Educ. 80 (5), 537, http://dx.doi.org/10.1021/ed080p537.

Winkler, L.W., 1888. Die Bestimmung des in Wasser gelösten Sauerstoffen. Berichte der Deutschen Chemischen Gesellschaft 21, 2843–2855.